

High-power, high-repetition-rate performance characteristics of β -BaB₂O₄ for single-pass picosecond ultraviolet generation at 266 nm

S. Chaitanya Kumar,^{1,*} J. Canals Casals,¹ Junxiong Wei,¹ and M. Ebrahim-Zadeh^{1,2}

¹ICFO-Institut de Ciències Fotoniques, Mediterranean Technology Park, 08860 Castelldefels, Barcelona, Spain

²Institució Catalana de Recerca i Estudis Avançats (ICREA), Passeig Lluís Companys 23, Barcelona 08010, Spain

*chaitanya.suddapalli@icfo.es

Abstract: We report a systematic study on the performance characteristics of a high-power, high-repetition-rate, picosecond ultraviolet (UV) source at 266 nm based on β -BaB₂O₄ (BBO). The source, based on single-pass fourth harmonic generation (FHG) of a compact Yb-fiber laser in a two-crystal spatial walk-off compensation scheme, generates up to 2.9 W of average power at 266 nm at a pulse repetition rate of ~80 MHz with a single-pass FHG efficiency of 35% from the green to UV. Detrimental issues such as thermal effects have been studied and confirmed by performing relevant measurements. Angular and temperature acceptance bandwidths in BBO for FHG to 266 nm are experimentally determined, indicating that the effective interaction length is limited by spatial walk-off and thermal gradients under high-power operation. The origin of dynamic color center formation due to two-photon absorption in BBO is investigated by measurements of intensity-dependent transmission at 266 nm. Using a suitable theoretical model, two-photon absorption coefficients as well as the color center densities have been estimated at different temperatures. The measurements show that the two-photon absorption coefficient in BBO at 266 nm is ~3.5 times lower at 200°C compared to that at room temperature. The long-term power stability as well as beam pointing stability is analyzed at different output power levels and focusing conditions. Using cylindrical optics, we have circularized the generated elliptic UV beam to a circularity of >90%. To our knowledge, this is the first time such high average powers and temperature-dependent two-photon absorption measurements at 266 nm are reported at repetition rates as high as ~80 MHz.

©2015 Optical Society of America

OCIS codes: (190.4360) Nonlinear optics, devices; (190.4400) Nonlinear optics, materials; (190.2620) Harmonic generation and mixing.

References and links

1. S. Orthaus, M. König, T. Schönau, V. Buschmann, S. Tannert, C. Lauritsen, F. Koberling, U. Ortmann, and R. Erdmann, "Crossing the limit towards deep UV," *Optik Photonik* **8**(1), 33–36 (2013).
2. Q. Li, T. Ruckstuhl, and S. Seeger, "Deep-UV laser-based fluorescence lifetime imaging microscopy of single molecules," *J. Phys. Chem. B* **108**(24), 8324–8329 (2004).
3. L. I. Isaenko, A. Dragomir, J. G. McInerney, and D. N. Nikogosyan, "Anisotropy of two-photon absorption in BBO at 264 nm," *Opt. Commun.* **198**(4-6), 433–438 (2001).
4. M. Ebrahim-Zadeh and S. C. Kumar, "Yb-Fiber-laser-pumped ultrafast frequency conversion sources from the mid-infrared to the ultraviolet," *IEEE J. Sel. Top. Quantum Electron.* **20**, 7600519 (2014).
5. D. N. Nikogosyan, *Nonlinear Optical Crystals: A Complete Survey* (Springer, 2005).
6. M. Takahashi, A. Osada, A. Dergachev, P. F. Moulton, M. Cadatal-Raduban, T. Shimizu, and N. Sarukura, "Improved fourth harmonic generation in β -BaB₂O₄ by tight elliptical focusing perpendicular to walk-off plane," *J. Cryst. Growth* **318**(1), 606–609 (2011).
7. R. Bhandari, T. Taira, A. Miyamoto, Y. Furukawa, and T. Tago, ">3MW peak power at 266 nm using Nd:YAG/Cr⁴⁺:YAG microchip laser and fluxless-BBO," *Opt. Mater. Express* **2**(7), 907–913 (2012).
8. S. Chaitanya Kumar, J. Canals Casals, E. Sanchez Bautista, K. Devi, and M. Ebrahim-Zadeh, "Yb-fiber-laser-based, 1.8 W average power, picosecond ultraviolet source at 266 nm," *Opt. Lett.* **40**(10), 2397–2400 (2015).

9. M. Takahashi, A. Osada, A. Dergachev, P. F. Moulton, M. Cadatal-Raduban, T. Shimizu, and N. Sarukura, "Effects of pulse rate and temperature on nonlinear absorption of pulsed 262-nm laser light in β -BaB₂O₄," *Jpn. J. Appl. Phys.* **49**(8), 080211 (2010).
10. M. Bradler and E. Riedle, "Sub-20 fs μ J-energy pulses tunable down to the near-UV from a 1 MHz Yb-fiber laser system," *Opt. Lett.* **39**(9), 2588–2591 (2014).
11. J. Rothhardt, S. Demmler, S. Hädrich, T. Peschel, J. Limpert, and A. Tünnermann, "Thermal effects in high average power optical parametric amplifiers," *Opt. Lett.* **38**(5), 763–765 (2013).
12. G. D. Boyd and D. A. Kleinman, "Parametric interaction of focused Gaussian light beams," *J. Appl. Phys.* **39**(8), 3597–3639 (1968).
13. S. Chaitanya Kumar, E. Sanchez Bautista, and M. Ebrahim-Zadeh, "Stable, high-power, Yb-fiber-based, picosecond ultraviolet generation at 355 nm using BiB₃O₆," *Opt. Lett.* **40**(3), 403–406 (2015).
14. D. Zhang, Y. Kong, and J. Zhang, "Optical parametric properties of 532-nm-pumped beta-barium-borate near the infrared absorption edge," *Opt. Commun.* **184**(5-6), 485–491 (2000).
15. D. Eimerl, L. Davis, S. Velsko, E. K. Graham, and A. Zalkin, "Optical, mechanical, and thermal properties of barium borate," *J. Appl. Phys.* **62**(5), 1968–1983 (1987).
16. C. D. Marshall, S. A. Payne, M. A. Hennesian, J. A. Speth, and H. T. Powell, "Ultraviolet-induced transient absorption in potassium dihydrogen phosphate and its influence on frequency conversion," *J. Opt. Soc. Am. B* **11**(5), 774–785 (1994).
17. M. Sheik-Bahae, A. A. Said, T. Wei, D. J. Hagan, and E. W. Van Stryland, "Sensitive measurement of optical nonlinearities using a single beam," *IEEE J. Quantum Electron.* **26**(4), 760–769 (1990).
18. S. C. Kumar, G. K. Samanta, K. Devi, and M. Ebrahim-Zadeh, "High-efficiency, multicrystal, single-pass, continuous-wave second harmonic generation," *Opt. Express* **19**(12), 11152–11169 (2011).

1. Introduction

High-power, ultrafast, picosecond sources in the ultraviolet (UV) are of great interest for a variety of scientific, industrial and medical application. In particular, high-repetition-rate MHz sources in the vicinity of 266 nm are interesting for confocal microscopy [1], single-molecule imaging [2] and optical characterization of materials [3]. Traditionally, access to this deep UV spectral range is best achieved by nonlinear frequency conversion techniques, such as fourth harmonic generation (FHG) of the well-established Nd:YAG or Yb-fiber lasers at 1064 nm. Fiber lasers offer several advantages over conventional solid-state lasers by providing powerful, yet compact, rugged, portable and air-cooled system architectures, which are desirable for many practical applications [4]. At the same time, the choice of suitable materials offering the required linear and nonlinear optical properties, in addition to the short-wavelength transmission cut-off, is a key factor for practical and efficient frequency conversion into the deep UV. The efficiency of the frequency conversion process depends critically on several material parameters, including effective nonlinear coefficient, spatial walk-off and phase-matching properties. Table 1 lists some key material parameters for frequency conversion into the deep UV in a number of prominent nonlinear crystals [5].

Table 1. Phase-matching properties of some prominent UV nonlinear crystals.

Nonlinear Crystal	UV Cutoff (nm)	Interaction	Phase-matching angle θ_{PM}°	d_{eff} (pm/V)	α_{UV} @ 266 nm (cm^{-1})	ρ (mrad)	Angular acceptance (mrad·cm)
BBO	180	Type-I ($oo \rightarrow e$)	47.56°	1.75	<0.17	85	0.19
CLBO	180	Type-I ($oo \rightarrow e$)	61.43°	0.76	-	33	0.47
KABO	180	Type-I ($oo \rightarrow e$)	56.79°	0.26	0.10	50.5	0.3
KBBF	160	Type-I ($oo \rightarrow e$)	36.37°	0.39	0.11	52.8	0.3
RBBF	170	Type-I ($oo \rightarrow e$)	39.97°	0.34	0.62	56.5	0.28

While most of these nonlinear crystals are not commercially available, β -BaB₂O₄ (BBO) and CsLiB₆O₁₀ (CLBO) are commonly used for UV generation at 266 nm. However, CLBO is known to be hygroscopic, requiring special precautions. On the other hand, BBO processes the highest nonlinearity of all the UV nonlinear crystals, with a nonlinear figure-of-merit ($FOM = d_{eff}^2/n^3$) ~ 0.65 pm²/V². In spite of constraints such as large spatial walk-off and narrow angular acceptance bandwidth, BBO has been widely used for FHG into the UV.

However, linear and two-photon absorption, as well as dynamic color center formation [6,7] in BBO, are significant limitations for high-power, high-repetition-rate UV generation, leading to thermal effects [8–11]. Hence, it is important to carefully study the performance characteristics of BBO for high-power, high-repetition-rate pulse generation in the UV at 266 nm.

In this study, we report high-average-power picosecond pulse generation at 266 nm based on single-pass FHG of a mode-locked Yb-fiber laser at 1064 nm, providing as much as 2.9 W of average UV power at ~80 MHz pulse repetition rate. Various measurements including angular and temperature acceptance bandwidths have been performed, and their effect on the interaction length are studied. Thermal effects have been systematically investigated. Nonlinear absorption in BBO has been determined by performing transmission measurements to estimate the two-photon absorption coefficients and the induced dynamic color centers in BBO at 266 nm at different temperatures. Long-term power and beam pointing stability measurements have been performed and analyzed. To our knowledge, this study is the first report on such high-average-power generation and temperature-dependent two-photon absorption measurements at 266 nm in BBO at repetition rates as high as ~80 MHz.

2. Experimental setup

The experimental setup for high-power, single-pass, picosecond UV generation is similar to that in Ref [8]. The fundamental source is a commercial mode-locked Yb-fiber laser (Femto Power, FP-1060-20) delivering up to 20 W of average power at 1064 nm in pulses of 20 ps duration at ~80 MHz repetition rate. The laser has a double-peaked spectrum with a full-width at half-maximum (FWHM) bandwidth of ~1.4 nm. The output power is adjusted using a combination of a half-wave plate and a polarizing beam-splitter cube. A second half-wave plate is used to obtain the required polarization for phase-matching in the frequency conversion crystals. The nonlinear crystal for second harmonic generation (SHG) is 30-mm-long LiB₃O₅ (LBO) with an aperture of 3 × 4 mm². It is cut at $\theta = 90^\circ$ ($\varphi = 0^\circ$) for type I ($oo \rightarrow e$) noncritical phase-matching (NCPM) along the optical x -axis. The end-faces of the crystal are antireflection (AR)-coated ($R < 0.1\%$) at 1064 and 532 nm. The crystal is mounted in an oven, which can be constantly maintained at the phase-matching temperature of 148.2°C with a stability of $\pm 0.1^\circ\text{C}$. The fundamental beam is focused at the center of the crystal to a waist radius of $w_F \sim 34 \mu\text{m}$, corresponding to a focusing parameter of $\xi_F \sim 2.74$ [12]. The generated SH green beam is separated from the residual fundamental using a pair of dichroic mirrors, MS, which are AR-coated for high transmission ($T > 99\%$) at 1064 nm and high reflection ($R > 99\%$) at 532 nm. The SHG stage provides as much as 9.1 W of average power at 532 nm for a fundamental power of 16.8 W at single-pass SHG conversion efficiency of 54% in 16.2 ps pulses with an excellent passive power stability better than 0.5% rms over 16 hours and a circular beam of high spatial quality [8,13]. After separation, the green beam is collimated using a lens, L₂, before entering the FHG stage. The BBO crystal for FHG is cut at $\theta = 47.56^\circ$ for type I ($oo \rightarrow e$) critical phase-matching to generate 266 nm in the UV. The end-faces of the crystal are AR-coated ($R < 0.1\%$) at 532 nm and 266 nm. The green beam from SHG stage is then focused using a lens, L₃, at the center of the BBO crystal for FHG at 266 nm. The generated UV radiation is then separated using another pair of the dichroic mirrors, MF, which are coated for high transmission ($T > 98\%$) at 532 nm and high reflection ($R > 99\%$) at 266 nm, and further filtered using FGUV5 glass.

3. Power scaling

In order to characterize our UV source, we initially performed the power scaling studies using two BBO crystals of lengths 5 and 10 mm. To achieve maximum FHG efficiency, careful optimization of the focusing condition was performed. Using the Boyd-Kleinman theory [12], we calculated the nonlinear coupling coefficient as a function of beam waist in the presence of spatial walk-off. The optimum SH beam waist to obtain maximum FHG efficiency was estimated to be $w_{SH1} \sim 13 \mu\text{m}$ for the 5-mm-long crystal and $w_{SH2} \sim 19 \mu\text{m}$ for the 10-mm-long

crystal, corresponding to focusing parameters of $\xi_{SH1} \sim 1.37$ and $\xi_{SH2} \sim 1.35$, respectively [12], indicating that the optimum focusing conditions for both crystal lengths are very close. Hence, we used a beam waist radius of $w_{SH} \sim 19 \mu\text{m}$ for both crystals [8]. The power scaling results for the picosecond UV source are shown in Fig. 1. Using the 5-mm-long BBO crystal, we were able to achieve a maximum UV average power of 1.4 W for an input green power of 8 W at a single-pass green to UV conversion efficiency of 18%, as shown in Fig. 1(a). The FH power is observed to increase quadratically, while the corresponding FHG efficiency has a linear dependence on the green power, as expected. Also shown in the inset of Fig. 1(a) is the variation of the FH power as a function of the square of the fundamental power, which is recorded to be linear, confirming the absence of any detrimental effects. Figure 1(b) shows the variation of the FH power and FHG efficiency with the input green power for the 10-mm-long crystal, where we were able to generate a maximum average FH power of 1.8 W for the same input green power of 8.4 W at a single-pass green to UV efficiency of 21.4%. A clear deviation in the linear behavior of the FHG efficiency is observed, particularly at high input green powers, leading to saturation in the FHG efficiency. The variation of the FH power as a function of the square of the green power, shown in the inset of Fig. 1(b), further indicates the saturation and presence of detrimental effects such as thermal loading. In order to verify the contribution of thermal effects in the 10-mm-long BBO crystal, we chopped the green beam at a frequency of 500 Hz with a 5.3% duty cycle, and repeated the power scaling measurements, the results of which are presented in Fig. 2. In presence of the chopper, the FH power varies quadratically with the green power, as expected, confirming the presence of thermal effects in the 10-mm-long crystal caused by the linear and nonlinear absorption at both the green and UV wavelengths in the absence of the chopper. This is also clear from the inset of Fig. 2, where the FH power is observed to grow linearly with the square of the input green power.

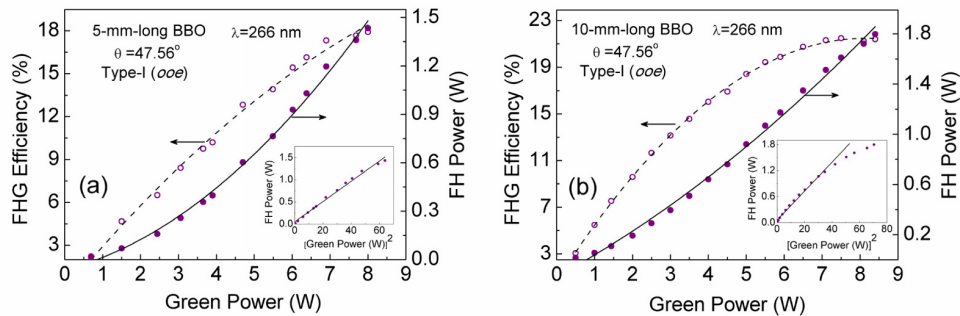


Fig. 1. Variation of the FH power and FHG efficiency as a function of the green power using (a) 5-mm-long and (b) 10-mm-long BBO crystals. Inset: Variation of the FH power as a function of the square of the green power.

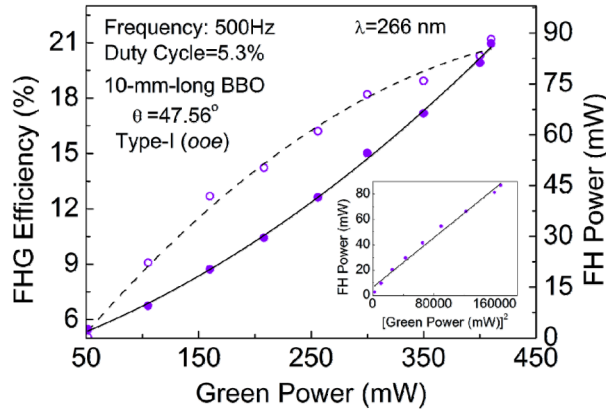


Fig. 2. Variation of the FH power and FHG efficiency as a function of the green power chopped at 5.3% duty cycle. Inset: Variation of the FH power as a function of the square of the chopped green power.

4. Walk-off compensation scheme

In order to further enhance the generated UV power, we used two 10-mm-long BBO crystals in walk-off compensation (WC) scheme. While the beam waist in the first crystal was maintained at $19 \mu\text{m}$, we used a pair of plano-concave mirrors with radius of curvature, $r = 200 \text{ mm}$, to focus the undepleted green power together with the generated UV output from the first crystal to a waist radius of $w_{\text{SH}} \sim 20 \mu\text{m}$ in the second crystal. Both BBO crystals were mounted on precision translation stages to account for any relative phase accumulation between the green and UV wavelengths. The separation between the crystals was optimized to achieve maximum UV power. The power scaling results for the two-crystal WC single-pass FHG scheme are shown in Fig. 3(a). For a maximum input green power of 8.2 W, we were able to generate as much as 2.9 W of UV power at a FHG conversion efficiency of 35% from green to UV. Although FHG efficiency increased linearly at low green powers, saturation is observed at higher power levels. Figure 3(b) shows the simultaneously measured power scaling results using the single crystal (SC) and the two-crystal WC schemes. As evident from Fig. 3(b) we were able to generate 1.8 W and 2.9 W of UV power after the first crystal and second WC crystal, respectively. This corresponds to $\sim 60\%$ enhancement in the UV power resulting from the WC scheme, as compared to the SC scheme at the maximum input green power. Also shown in the inset of Fig. 3(b) is the variation of the FH power enhancement and the enhancement factor as a function of the green power. The FH power enhancement varies from 13 mW at low power to a maximum of $\sim 1.1 \text{ W}$ at high power, with almost constant enhancement factor of 1.5-1.6 for all green powers. The relatively low enhancement in the WC scheme could be attributed to the strong focusing in the two nonlinear crystals limiting the effective interaction length.

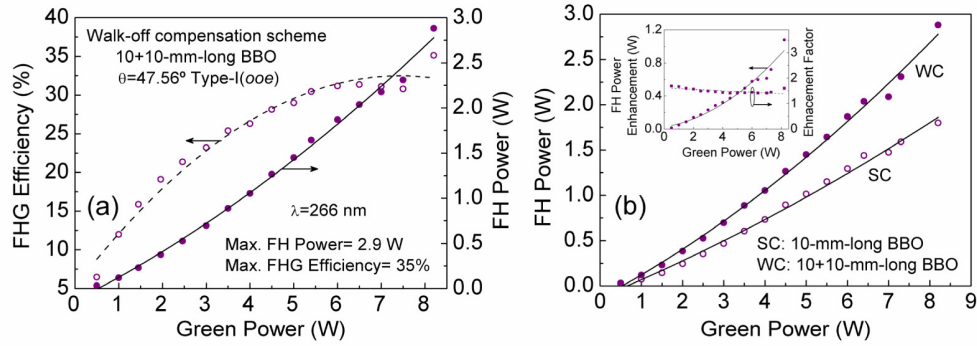


Fig. 3. (a) FH power and efficiency scaling as a function of the input green power using two 10-mm-long BBO crystals in walk-off compensation configuration. (b) Simultaneously measured SH power after the first crystal (SC) and second walk-off compensation crystal (WC), Inset: variation of FH power enhancement and enhancement factor as a function of input green power.

5. Angular acceptance bandwidth for FHG in BBO

In order to study the phase-matching properties of BBO for FHG into the UV at 266 nm, we performed angular acceptance measurements in both BBO crystals under different focusing conditions. The variation of the normalized FH power as a function of the internal angular deviation about the phase-matching angle for the two crystals is presented in Fig. 4. We performed these measurements at relatively low average powers to avoid thermal effects. The angular acceptance bandwidths were determined for the 5-mm-long and 10-mm-long crystals under two different focusing conditions of $w_{SH} \sim 55 \mu\text{m}$ and $w_{SH} \sim 19 \mu\text{m}$, respectively. As can be seen in Figs. 4(a)-4(d), the FWHM angular acceptance bandwidth is measured to be $\Delta\theta = 1.5$ mrad and $\Delta\theta = 4.1$ mrad for the 5 mm crystal, and $\Delta\theta = 1.9$ mrad and $\Delta\theta = 4.8$ mrad for the 10 mm crystal, for $w_{SH} \sim 55 \mu\text{m}$ and $w_{SH} \sim 19 \mu\text{m}$, respectively. The solid dots in the plots are the experimental measurements, while the solid curve corresponds to the sinc^2 fit to the data. These values are significantly wider than the theoretically calculated values of ~ 0.3 mrad and ~ 0.2 mrad for 5 and 10 mm crystals, respectively, using the relevant Sellmeier equations [14]. This deviation of the experimentally measured values from the theoretical calculation is attributed to the reduced effective interaction length due to spatial walk-off in BBO. The green beam waist radii of $w_{SH} \sim 55 \mu\text{m}$ and $w_{SH} \sim 19 \mu\text{m}$ correspond to confocal parameters of $b \sim 6$ cm and 0.7 cm, respectively. However, considering a spatial walk-off of $\rho = 85$ mrad, the effective interaction length reduces to $L_{\text{eff}} = 1.1$ mm for $w_{SH} \sim 55 \mu\text{m}$ and 0.4 mm for $w_{SH} \sim 19 \mu\text{m}$. The theoretically calculated normalized FH power as a function of internal angular deviation for a walk-off-limited effective length, $L_{\text{eff}} = 1.1$ mm and 0.4 mm, is shown in Figs. 4(e) and 4(f), resulting in a FWHM angular acceptance bandwidth of 1.5 mrad and 4.1 mrad, which are in excellent agreement with the experimentally measured values for the 5-mm-long BBO crystal, while a small deviation can be observed for the 10-mm-long crystal. Another limiting factor for the interaction length could be the temporal walk-off between the green and UV pulses, which is calculated to be 568 fs/mm. This results in a temporal walk-off limited interaction length of ~ 28 mm, which is much longer than the physical length of the crystal. Hence, as evident from the measurements presented in Figs. 4(a)-4(d), the effective interaction length is mainly limited by the spatial walk-off in the BBO crystal.

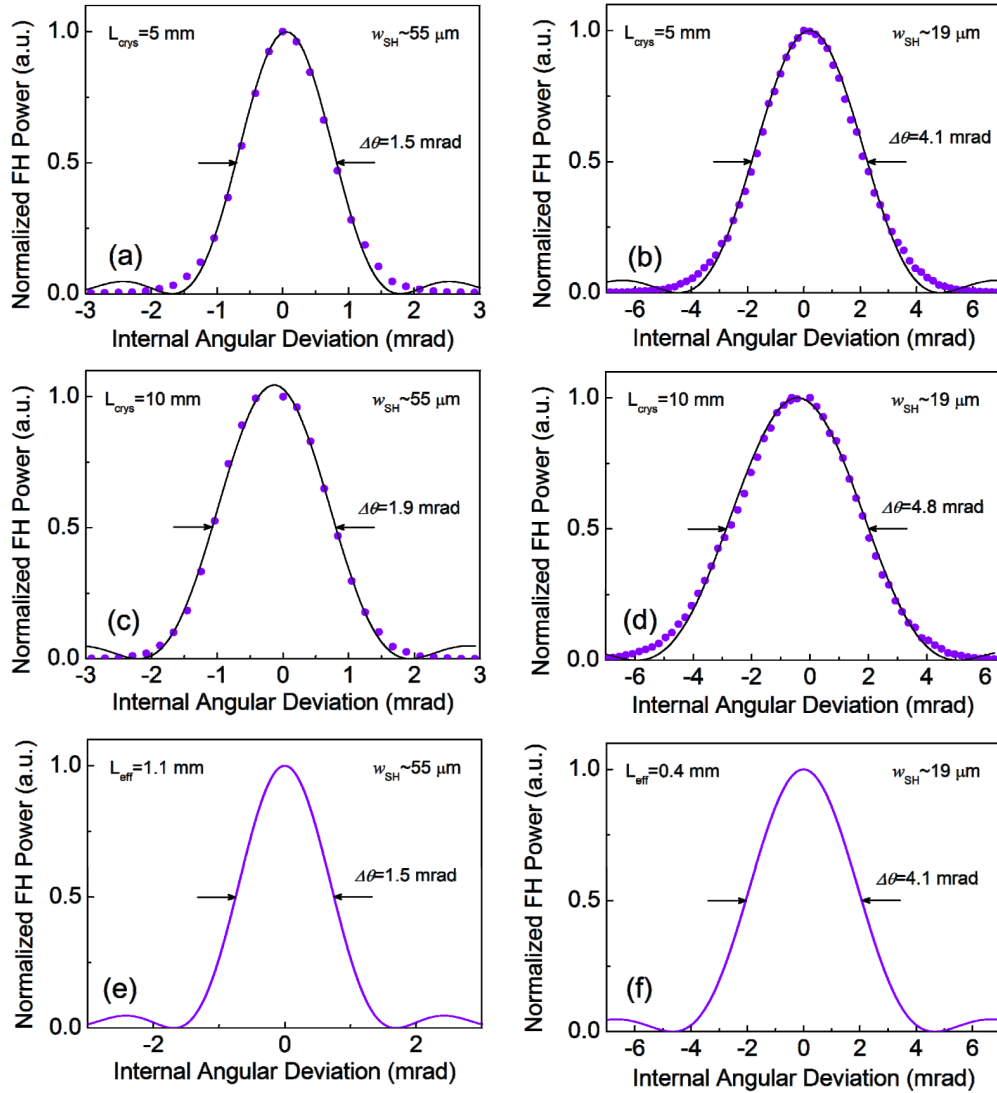


Fig. 4. (a-d) Experimentally measured, and (e,f) theoretically calculated angular acceptance bandwidth for 5-mm-long and 10-mm-long BBO crystals under two different focusing conditions for FHG into the UV at 266 nm.

6. Temperature acceptance bandwidth and thermal effects

We further investigated the temperature acceptance of the 10-mm-long crystal under the loose focusing condition with $w_{SH} \sim 55 \mu\text{m}$. The normalized FH power as a function of the temperature deviation about the phase-matching temperature is shown in Fig. 5(a), where it can be seen that the sinc^2 fit to the experimental data resulted in a FWHM temperature acceptance bandwidth of $\Delta T = 33^\circ\text{C}$. This is much wider than the theoretically estimated bandwidth of $\Delta T = 5.3^\circ\text{C}$ for a 10-mm-long BBO crystal using the temperature-dependent Sellmeier equations [14,15]. The experimentally measured bandwidth corresponds to a temperature bandwidth-limited interaction length of 1.6 mm, as shown in Fig. 5(b), which is slightly larger than the walk-off limited interaction length of $L_{\text{eff}} = 1.1 \text{ mm}$ under identical focusing condition. Although the effective interaction length for UV generation is only 1.1 mm, the entire physical length of the crystal contributes to the absorption at both green and

UV wavelengths. Hence, the increased interaction length estimated from the temperature bandwidth measurements could be attributed to thermal gradients in the crystal. These thermal gradients could be caused by the non-uniform heating of the crystal, given the large volume, and because of the local temperature rise due to linear and nonlinear absorption in the crystal at both green and UV wavelengths. In order to confirm possible thermal gradients due to absorption at the interacting wavelengths, we directly measured the temperature at the surface of the 10-mm-long BBO crystal at room temperature. The results are presented in Fig. 6, where it can be seen that as the input green power is increased, the UV power increases simultaneously, also increasing the temperature at the center of the BBO crystal from 21.8°C at low power to a maximum of 27.9°C at ~1.7 W of generated UV power. During this measurement, the BBO crystal remained at the optimum phase-matching angle to generate maximum UV power, with the green beam in *ordinary* polarization (*o*-polarization) and focused to a waist radius of $w_{SH} \sim 19 \mu\text{m}$, while the generated UV beam was of *extraordinary* polarization (*e*-polarization). The measurement confirms a significant rise in the crystal temperature caused by both green and UV wavelengths. In order to decouple the contributions of the green and UV wavelengths to the temperature rise, we changed the angle of the crystal out of phase-matching and performed the same measurement in the presence of green beam (*o*-polarization) without generating UV. This is shown in the inset (a) of Fig. 6, where it can be seen that the temperature rises very slowly from 21.8°C at low power to 22.1°C at ~8.3 W of green. A similar measurement using another 10-mm-long BBO crystal was performed for the UV beam (*e*-polarization), with the results shown in the inset (b) of Fig. 6. As can be seen, the temperature rises from 21.8°C at low UV power to 23.1°C at a maximum UV power of ~1.2 W. From these measurements, it is clear that the temperature rise due to the UV beam alone is higher than that of the green beam, but significantly lower than the combined temperature rise. Further, we also measured the temperature towards the end-faces of the crystal, under optimum phase-matching condition, resulting in an asymmetric/non-uniform increase, with the temperature at the output face of the crystal 50% higher than that at the input face, indicating the presence of thermal gradients.

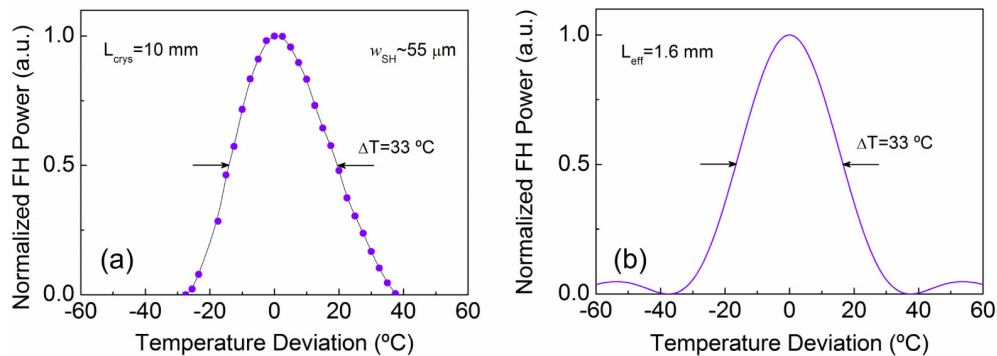


Fig. 5. (a). Experimentally measured, and (b) theoretically calculated temperature acceptance bandwidth of 10-mm-long BBO crystal for FHG into the UV at 266 nm.

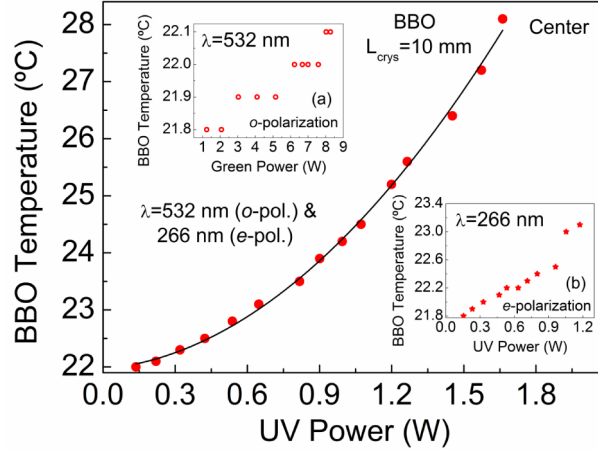


Fig. 6. Variation of the temperature measured directly at the center of the BBO crystal at room temperature, due to absorption at the green and UV wavelengths. Inset: Temperature rise due to (a) green, and (b) UV, independently.

7. Two-photon absorption at 266 nm in BBO

The above temperature measurements in the BBO crystal indicate significant contribution of thermal effects from the generated UV beam. Moreover, BBO is known to exhibit two-photon absorption or dynamic color center formation, particularly when generating UV radiation at 266 nm [6], which could be a serious limiting factor at repetition rates as high as ~80 MHz used in this work. Hence, to further study these UV-induced thermal effects, we performed transmission measurements at different temperatures using the 10-mm-long BBO crystal to estimate the two-photon absorption coefficient in BBO. The variation of the transmission of the BBO crystal as a function of the input UV intensity at a temperature of 22°C, 100°C, and 200°C are shown in Figs. 7(a)-7(c) respectively, for a UV beam waist radius of $w_{UV} \sim 15 \times 104 \mu\text{m}$. We used a simple theoretical model by considering a Gaussian temporal profile for the UV pulses in the presence of linear absorption, and assuming the formation of dynamic color-centers due to two-photon absorption in BBO, to model the defect densities, while also considering the bleaching of the color centers over the entire pulse duration to be negligible [16]. The equations governing the color center densities and the UV intensity through the BBO crystal are given by,

$$\frac{dN(z,t)}{dt} = \frac{\beta I_{4\omega}^2(z,t)}{8\hbar\omega} \quad (1)$$

$$\frac{dI_{4\omega}(z,t)}{dz} = -\{\alpha + N(z,t)\sigma_{4\omega}\}I_{4\omega}(z,t) - \beta I_{4\omega}^2(z,t) \quad (2)$$

where N is the color center density, $I_{4\omega}$ is the UV intensity, α , β are the linear and two-photon absorption coefficients at 266 nm and $\sigma_{4\omega}$ is the defect absorption cross-section. Using the relevant parameters and $\sigma_{4\omega} = 8 \times 10^{-17} \text{ cm}^2$ along with the experimentally measured transmission data, we estimated the two-photon absorption coefficients to be $\beta = 3.9 \text{ cm/GW}$ at 22°C, $\beta = 2 \text{ cm/GW}$ at 100°C, and $\beta = 1.1 \text{ cm/GW}$ at 200°C. As evident from Figs. 7(a)-7(c), the value of the two-photon absorption coefficient at 200°C is ~3.5 times lower than that at room temperature. Further improvements in the accuracy of two-photon absorption coefficient values at different temperatures can be achieved by using sensitive measurements techniques such as Z-scan [17]. Considering the density ($\rho = 3.85 \times 10^6 \text{ g/m}^3$), specific heat ($C_p = 490 \times 10^{-3} \text{ J/g-K}$), and thermal conductivity ($K = 1.6 \text{ W/m-K}$) for BBO, we determined the characteristic thermal relaxation time to be 53 μs [5]. Given the ~80 MHz repetition rate,

corresponding to a time interval of 12.5 ns between the generated UV pulses, the linear and two-photon absorption lead to accumulated thermal effects. The corresponding variation of the color center density as a function of the intensity for a single pulse is shown in Fig. 7(d). The color center density is found to reduce by ~44% and ~69% while operating at 100°C and 200°C, respectively, as compared to that at room temperature, for a maximum UV intensity of 45.7 mW/cm², confirming the contribution of two-photon absorption to color center formation in BBO.

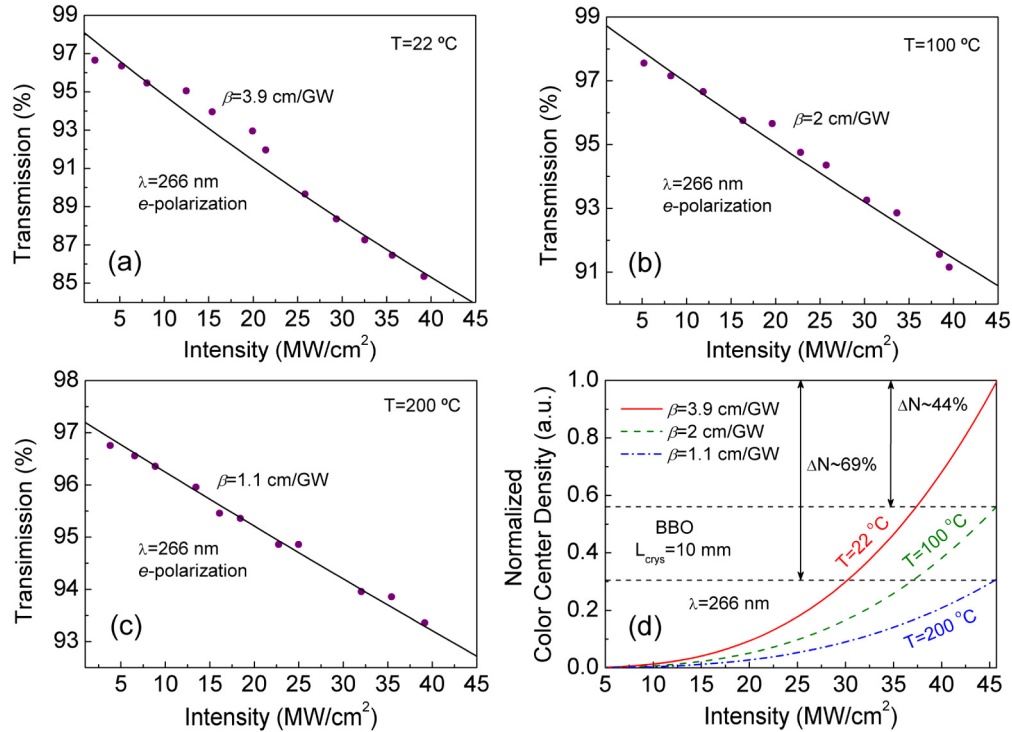


Fig. 7. Variation of the BBO transmission at 266 nm as a function of the intensity at (a) 22°C, (b) 100°C, and (c) 200°C. Solid circles and solid lines correspond to experimental data and theory, respectively. (d) Variation of the normalized color center density as a function of UV intensity at different temperatures.

8. Long-term UV power stability

We also performed long-term power stability measurements of the generated UV radiation at 266 nm with both BBO crystals. The passive power stability of the picosecond UV output beam at an arbitrary power level with the 5-mm-long crystal, measured over more than 12 hours at a temperature of 22°C, and in comparison to that at 100°C, is shown in Fig. 8(a). As can be seen, the UV power drops rapidly from 1.15 W down to 0.4 W after 6 hours when operating at a temperature of 22°C, while the decline is slower when the BBO crystal is heated to a temperature of 100°C. By translating the crystal to focus the input green beam at a new position inside the BBO crystal, we could readily recover the maximum UV power. The stability and the variation of the UV power over the initial 2 hours are clearly shown in the inset of Fig. 8(a). We further recorded the passive long-term power stability of the generated UV output at an arbitrary power level of 1.5 W over 16 hours using the 10-mm-long BBO crystal at an operating temperature of 200°C. As can be seen in Fig. 8(b), the UV power exhibits a long-term drift, resulting in a slow decline from 1.5 W down to ~1 W after 16 hours. Nevertheless, the UV power is recorded to exhibit passive power stability better than 3% rms over >8 hours, as shown in the inset of Fig. 8(b). No damage has been observed in the

BBO crystal even after such long-term operation. However, we have observed AR coating damage on the exit face of the crystal after sufficiently long-term operation at high power. The improvement in the long-term stability could be attributed to the reduced two-photon absorption coefficient, and hence the dynamic color center formation, at high temperatures.

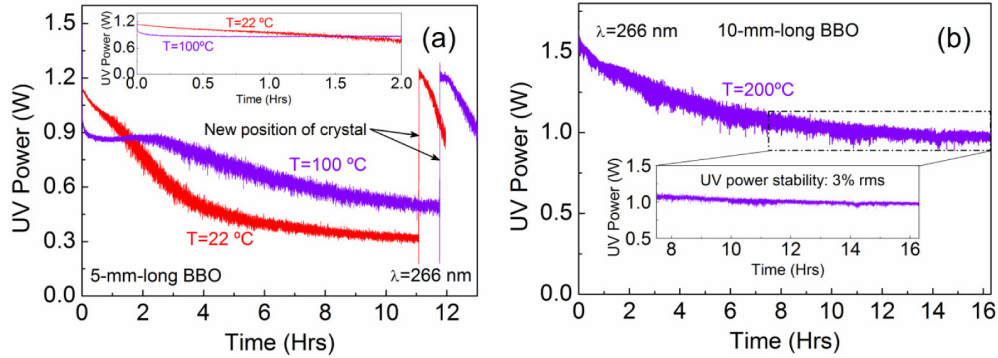


Fig. 8. Long-term power stability of the generated UV output using (a) 5-mm-long, and (b) 10-mm-long BBO.

9. UV Beam pointing stability

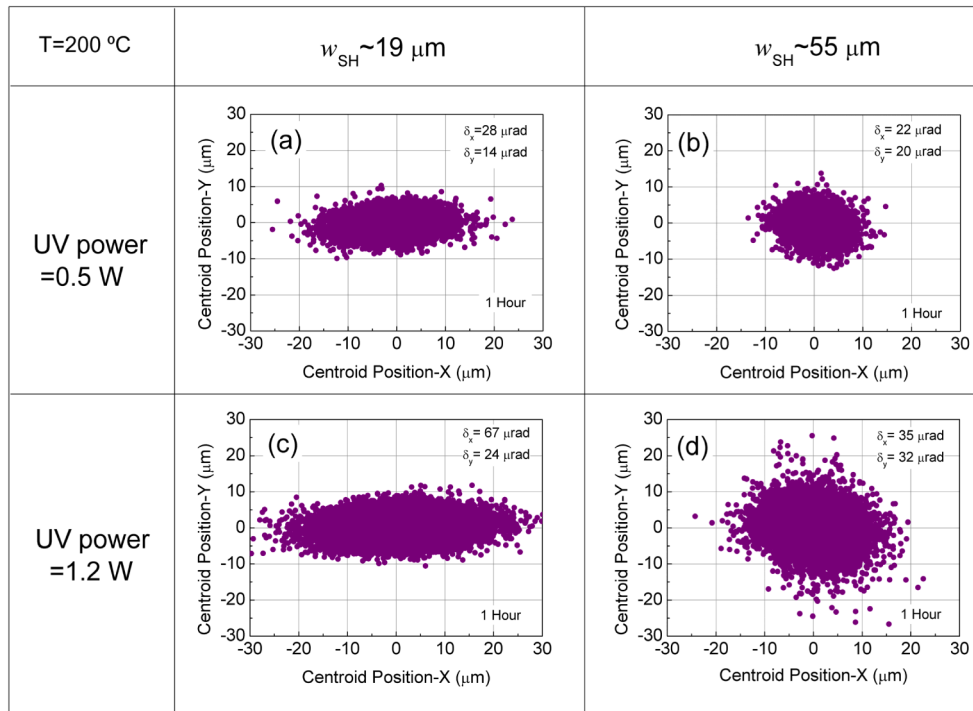


Fig. 9. UV beam pointing stability measurements performed at a temperature of 200°C for (a) UV power = 0.5 W, $w_{SH} \sim 19 \mu\text{m}$, (b) UV power = 0.5 W, $w_{SH} \sim 55 \mu\text{m}$, (c) UV power = 1.2 W, $w_{SH} \sim 19 \mu\text{m}$, and (d) UV power = 1.2 W, $w_{SH} \sim 55 \mu\text{m}$.

We also performed beam pointing stability measurements of the generated UV and studied the effect of green beam focusing on the pointing stability at different UV output power levels. In order to improve the stability and minimize the effects due to absorption, we

operated the BBO crystal at a temperature of 200°C. These results are presented in Figs. 9(a)-9(d). When the green beam is focused to a beam waist of $w_{SH} \sim 19 \mu\text{m}$, the generated UV beam is recorded to exhibit an asymmetric pointing stability with $<28 \mu\text{rad}$ in x -direction and $<14 \mu\text{rad}$ in y -direction while generating 0.5 W of UV, and with $<67 \mu\text{rad}$ in x -direction and $<24 \mu\text{rad}$ in y -direction while generating 1.2 W of UV power. Similar measurements using the more relaxed green beam waist of $w_{SH} \sim 55 \mu\text{m}$ resulted in a relatively symmetric pointing stability in both directions, with $<22 \mu\text{rad}$ in x -direction and $<20 \mu\text{rad}$ in y -direction while generating 0.5 W of UV, and with $<35 \mu\text{rad}$ in x -direction and $<32 \mu\text{rad}$ in y -direction while generating 1.2 W of UV power. These measurements indicate that using a loose focusing condition for generating the same amount of UV power improves the output beam pointing stability.

10. UV Beam profile

Using the 10-mm-long BBO crystal and green beam waist radius of $w_{SH} \sim 55 \mu\text{m}$, we also recorded the far-field energy distribution of the generated UV beam at an output power of ~ 1.3 W. Owing to the large spatial walk-off of $\rho = 85 \text{ mrad}$ in the BBO crystal, the generated UV beam at the output of the FHG stage is elliptic, as shown in Fig. 10(a). The diameters of the elliptic UV beam in Fig. 10 (a) are 4.9 mm along the major axis and 1 mm along the minor axis, corresponding to a circularity of $\sim 20\%$. However, we were able to readily circularize the beam using suitable cylindrical optics. We used a pair of UV fused silica cylindrical lenses of focal length $f = 100$ mm and 75 mm, separated by ~ 26 cm, to circularize the elliptic beam. The far-field energy distribution of the circularized UV beam, together with the orthogonal intensity profiles, measured at ~ 1 m from the FHG stage, is shown Fig. 10(b).

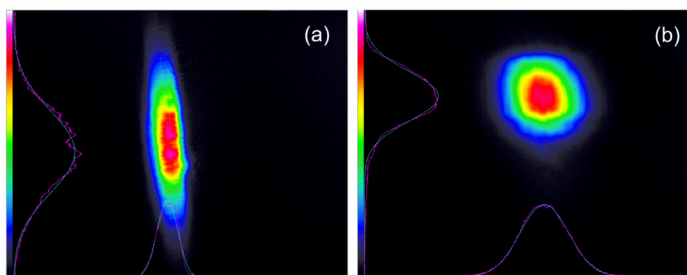


Fig. 10. Spatial beam profile of the (a) generated, and (b) circularized UV radiation at 266 nm in BBO.

The beam diameters for the circularized UV beam are measured to be 2.6 mm along the major axis and 2.4 mm along the minor axis, corresponding to circularity of $\sim 90\%$ over ~ 1 m.

11. Spectrum and pulse train

We also measured the spectrum of the UV output beam using a spectrometer with a resolution of 0.5 nm. The result is shown in Fig. 11(a), confirming a central wavelength of 266 nm with a bandwidth of ~ 0.9 nm (FWHM), limited by the instrument resolution. Figure 11(b) depicts the UV pulse train obtained using silicon photodetector. As can be seen, the UV pulses are separated by 12.5 ns, corresponding to a pulse repetition rate of ~ 80 MHz, as expected.

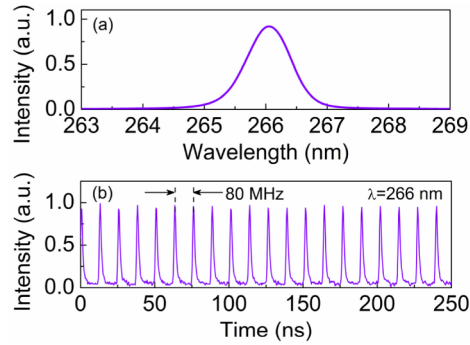


Fig. 11. (a) Spectrum centered at 266 nm, and (b) pulse train of the generated UV radiation at 266 nm.

12. Conclusions

In conclusion, we demonstrated a high-power, high-repetition-rate, picosecond UV source at 266 nm based on single-pass FHG in BBO. We compared the performance of UV source using two BBO crystals of lengths 5 mm and 10 mm, generating a maximum UV average power of 1.8 W at ~ 80 MHz for an input green power of 8.4 W at a single-pass green to UV conversion efficiency of 21.4%. By deploying a two-crystal WC scheme, we were able to improve the generated UV power by $>60\%$ to 2.9 W at a single-pass FHG efficiency of 35% from green to the UV. We performed detailed characterization of the phase-matching properties of the BBO crystal for UV generation at 266 nm and found that the angular acceptance bandwidth is essentially determined by the walk-off limited interaction length. The temperature acceptance bandwidth measurements revealed a slightly longer interaction length potentially caused by the thermal gradients due to linear and nonlinear absorption at the green as well as the UV wavelength. Further, we investigated the origin of thermal effects due to the nonlinear absorption and dynamic color center formation by performing transmission measurements of BBO crystal at 266 nm and estimated the two-photon absorption coefficients at different temperatures using a suitable theoretical model. These measurements showed significant drop in color center density at high temperatures induced by two-photon absorption, while the two-photon absorption coefficient itself in BBO at 266 nm decreased by ~ 3.5 times at 200°C as compared to that at room temperature. We also performed long-term power stability analysis at various temperatures resulting in a passive UV power stability better than 3% rms over >8 hours. Although two-photon absorption and induced dynamic color center formation could be identified as a one of the causes for the UV power instability, further investigation is required to establish additional factors. The drastic temperature rise on the surface of the crystal while generating high UV power, as compared to the independent temperature rise due the green and UV, could be considered as an indication of some induced effects. The pointing stability measurements indicate better performance when loose focusing of $w_{\text{SH}} \sim 55 \mu\text{m}$ is deployed, as compared to a tight focusing of $w_{\text{SH}} \sim 19 \mu\text{m}$, while generating the same amount of UV power. Nevertheless, the UV beam exhibits a beam pointing stability $< 35 \mu\text{rad}$ at 1.2 W of UV output power. Despite the elliptic nature of the generated UV beam due the spatial walk-off in BBO, we used cylindrical optics to circularize the beam, obtaining a circularity of $>90\%$. Further improvements in the UV output power could be expected by using fluxless BBO with improved crystal quality [7], multiple short crystals [18], and elliptic focusing [6,13].

Acknowledgments

We acknowledge support from the Ministry of Economy and Competitiveness (MINECO), Spain, through project OPTEx (TEC2012-37853).